Hindawi
International Journal of Antennas and Propagation
Volume 2021, Article ID 6035169, 13 pages
https://doi.org/10.1155/2021/6035169

*Research Article*

# Small Triple-Band Meandered PIFA for Brain-Implantable Biotelemetric Systems: Development and Testing in a Liquid Phantom

**Nikta Pournoori**,[1] **Lauri Sydänheimo**,[1] **Yahya Rahmat-Samii**,[2] **Leena Ukkonen**,[1] **and Toni Björninen**[3]

[1]*Faculty of Medicine and Health Technology, Tampere University, Tampere, Finland*
[2]*Department of Electrical and Computer Engineering, University of California, Los Angeles (UCLA), Los Angeles, CA, USA*
[3]*Faculty of Information Technology and Communication Sciences, Tampere University, Tampere, Finland*

Correspondence should be addressed to Nikta Pournoori; nikta.pournoori@tuni.fi

Received 16 June 2021; Revised 25 September 2021; Accepted 29 October 2021; Published 28 November 2021

Academic Editor: Mohammad Alibakhshikenari



We present a meandered triple-band planar-inverted-F antenna (PIFA) for integration into brain-implantable biotelemetric systems. The target applications are wireless data communication, far-field wireless power transfer, and switching control between sleep/wake-up mode at the Medical Device Radiocommunication Service (MedRadio) band (401–406 MHz) and Industrial, Scientific and Medical (ISM) bands (902–928 MHz and 2400–2483.5 MHz), respectively. By embedding meandered slots into the radiator and shorting it to the ground, we downsized the antenna to the volume of $11 \times 20.5 \times 1.8$ mm$^3$. We optimized the antenna using a 7-layer numerical human head model using full-wave electromagnetic field simulation. In the simulation, we placed the implant in the cerebrospinal fluid (CSF) at a depth of 13.25 mm from the body surface, which is deeper than in most works on implantable antennas. We manufactured and tested the antenna in a liquid phantom which we replicated in the simulator for further comparison. The measured gain of the antenna reached the state-of-the-art values of −43.6 dBi, −25.8 dBi, and −20.1 dBi at 402 MHz, 902 MHz, and 2400 MHz, respectively.

## 1. Introduction

Implantable wireless medical devices are a major focus of health technology development. They enable the minimally intrusive long-term monitoring and management of medical conditions [1–7]. This conception has sparked the research on antennas and wireless technology that meets the demands of modern medical applications [1–6], and multiple frequency bands have become available for wireless implant communications. Among them are MedRadio at the frequency range of 401–406, 413–419, 426–432, 438–444, and 451–457 MHz and the ISM bands of 433.1–434.8 MHz, 868–868.6 MHz, 902.8–928.0 MHz, and 2.4–2.48 GHz [8]. Figure 1 shows an overview of wireless brain implant communication for continuous human health monitoring applications.

During the past decade, the research on implantable antennas has evolved and expanded rapidly. The advancements include both new knowledge on the fundamental features and limitations to antennas in the biological environment [9–13], as well as numerous practical demonstrations [14–17]. Since an implantable device must be small to minimize its intrusiveness, the antenna's size-performance balance must be emphasized in the design. At the same time, the electrical size of the antenna cannot be increased by using higher frequencies, e.g., cm- or even mm-wave regime, because the path loss in the biological media becomes infeasibly high beyond the low GHz range [10, 12]. Thus, implantable antennas are electrically small, which makes the design of the antenna-enabled biomedical telemetry a challenging aim. In addition, there is a growing need for more versatile, multiband/modal implantable

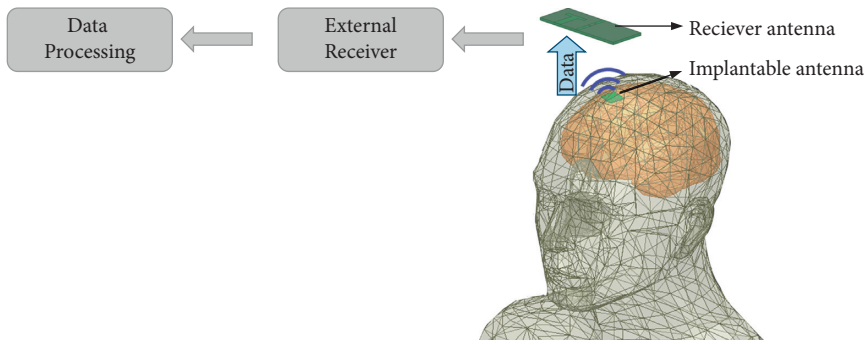


Figure 1: An overview of wireless brain implant communication.

antenna systems that meet the demands of modern wireless communications systems. As a result, implantable antennas that support wireless powering, data transmission, and control signaling at multiple frequency bands have become an important trend of the research. Among the studied antenna structures, PIFA has been found promising due to its adaptable structure that eases the design and competitive size-performance balance in the lossy tissue environment [18–21].

For implant antenna miniaturization, plenty of techniques have been employed. Shah et al. [22] have reported a triple-band antenna based on a spiral-shaped radiator fed through a slotted ground plane. The antenna has a small volume of 17.5 $mm^3$. When implanted at a depth of 3 mm in the scalp, it provided the gain values of −30.5, −22.6, and −18.2 dBi, respectively. A similar approach, based on a spiral-shaped radiator and slotted ground plane, was used by Shang et al. [23] to create a bandwidth-enhanced dual-band PIFA that was subcutaneously implanted at a depth of 3 mm. The antenna achieved the fractional bandwidths of 38% and 6.9% and gain values of −38.8 dBi and −18.6 dBi at 402 MHz and 2.45 GHz, respectively. In [24], Gani and Yoo introduced a scalp-implantable meandered PIFA with a compact size of 52.5 $mm^3$ resonating at 405, 915, and 2450 MHz. In [25], Faisel et al. developed a dual-resonant square-shaped PIFA in the volume of 9.8 $mm^3$ (915 and 2450 MHz) as a part of a scalp-implanted biotelemetry device. Both antennas [24, 25] enabled the data telemetry, wireless power transfer, and wake-up signal operation for intracranial pressure (ICP) monitoring with adequate gain values (−40.9, −33.0, and −22.4 dBi at 405, 915, and 2450 MHz [24] and −27.7 and −23.0 dBi at 915 and 2450 MHz [25]). However, they were not implanted within the cranial cavity but at the depth of 3 mm in the scalp. The authors of [26–29] introduced 3-layer stacked PIFAs to achieve broad impedance bandwidth within a small antenna volume. However, this improvement was achieved at the cost of increasing the antenna's thickness and weight and complicating the fabrication process.

In our earlier numerical study [30], we introduced a dual-resonant implantable PIFA with the size of $11 \times 19 \times 1.25\ mm^3$ where we utilized a slotted radiator and attained the simulated antenna gain of −26.7 and −17.5 dBi at 902 and 2400 MHz, respectively. In the further numerical study [31, 32], we developed a meandered radiator in the antenna that provided a third resonance at 402 MHz with the simulated antenna gain of −42.3, −24.2, and −21.6 dBi at 402, 902, and 2400 MHz, respectively, with the antenna size of $12.6 \times 19 \times 1.25\ mm^3$. Since the antenna's width and length impact its radiation performance profoundly, here, we slightly increased the length and reduced the width compared to our previous studies. This change reduced the antenna's cross-sectional area by 5.8%. This way, we were able to provide longer electrical characteristics for both radiating and ground planes and elevate the radiation intensity of the antenna, specifically at the lower frequency band. Additionally, to provide impedance fine-tuning, we evaluated other crucial design parameters, including the lengths of the meandered slots and shorting strip and the feeding port's location. Therefore, in this work, we have optimized the antenna's radiation performance further at the lowest operating frequency of 402 MHz achieving a 3.9 dB improvement in the gain at the same implant depth of 13.25 mm without considerably increasing its size. As a further advancement to previous numerical studies [30–32], in this article, we also present measured results obtained in a liquid phantom utilizing a plastic truncated cone-shaped container to validate the antenna's performance experimentally. Moreover, to better compare the measurement and simulation results, we replicated the plastic container with tissue-mimicking liquid in the HFSS. In addition, we have assessed the specific absorption rate of the antenna through simulations. Finally, we review the gain of several implantable antennas versus the electrical size ($ka$) at their lowest operating frequency. Our proposed antenna ($ka = 0.09$) is implanted between 3.25 mm and 10.25 mm deeper than all other dual or triple-band antennas except for [18], which has higher $ka$ of 0.14. Based on this comparison, our antenna achieves a compelling size-performance balance at a depth that enables brain-implantable bio-telemetric systems operating within the cranial cavity.

## 2. Antenna Development and Numerical Models

*2.1. Design Principles.* Figures 2(a) and 2(b) depict the configuration and geometry of the proposed miniaturized triple-band PIFA with meandered slots, respectively. A shorting strip vertically connects the meandered radiating patch to the ground layer in the $y$-$z$ coordinate plane, and a 50-Ω coaxial cable feeds the antenna via a pin with a 0.6 mm radius embedded into the radiator at the distance of 7.8 mm

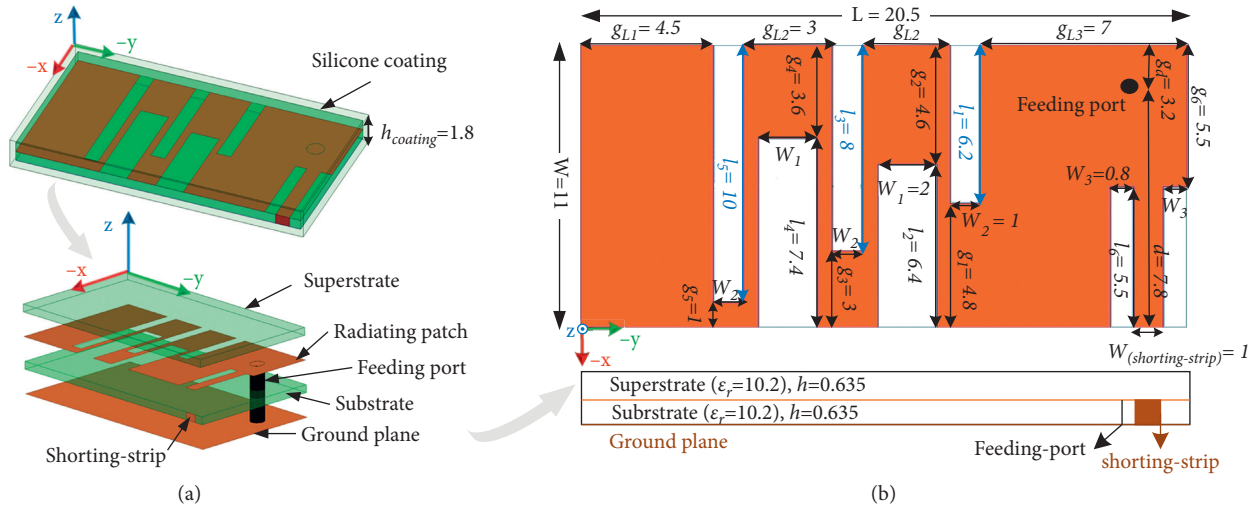


FIGURE 2: The proposed meandered triple-band implantable PIFA configuration. (a) The structure of the proposed PIFA and (b) its geometrical parameters (all dimensional parameters are given in the units of millimeters).

($d$) from shorting strip. Initially, we estimated the dimension of the radiator to operate at the 902 MHz resonant frequency of the ISM band utilizing given equation (1) in free space [33–36].

$$f = \frac{C_0}{4\sqrt{\varepsilon_r}\left(L + W + h - W_{(\text{Shorting-Strip})}\right)}, \quad (1)$$

where $C_0$ is the speed of light in free space, $\varepsilon_r$ is the relative permittivity of the substrate, $L$ and $W$ denote the length and width of the radiating element, respectively, $h$ is the thickness of the substrate, and $W_{(\text{shorting-strip})}$ is the shorting strip width. Based on this equation, high-permittivity substrate and superstrate layers (Rogers RO3210; $\varepsilon_r = 10.2$, $\tan\delta = 0.003$, $h = 0.635$ mm) help to lower the resonance frequency. To use this initial design in free space inside the human tissues, we covered the radiator with a superstrate layer to insulate the implantable antenna from the surrounding biological tissues and improve its radiation characteristics. Additionally, we applied silicone-coating (MED-2000, Avantor Inc., U.S.; $\varepsilon_r = 2.2$, $\tan\delta = 0.007$, $h_{\text{coating}} = 1.8$ mm) all around the layers to preserve biocompatibility. In the second step, we employed several slots ($l_2$, $l_3$, $l_4$, and $l_5$) on the radiating patch to further decrease the antenna's volume and broaden its bandwidth. Afterward, to generate resonance at the MedRadio band, it was required to lengthen the effective current-flow path on the radiator through meandering these cutting slots ($l_2$, $l_3$, $l_4$, and $l_5$).

Finally, we inserted one more meandered slot ($l_1$) close to the antenna's feeding probe to create the resonance at 2400 MHz. However, in this approach, we generated an additional fourth resonance near 1600 MHz. In the future, we will explore the possibility of shifting this resonance to cover the 1395–1400 MHz and 1427–1432 MHz Wireless Medical Telemetry Service (WMTS) bands to achieve a quad-band implantable antenna. Consequently, compact triple-band PIFA by embedment of several meandered slots demonstrates attractive features for multitasking biotelemetry systems.

*2.2. Simulation Setups and Environment.* The numerical simulations were conducted on an ANSYS High Frequency Structure Simulator (HFSS) based on the finite element method. In antenna optimization, we used a 7-layer human head model made up of rectangular-shaped tissue layers, as illustrated in Figure 3. Based on [37–39], we selected the thickness of 2 mm for skin, fat, and muscle layers. The thickness of the dura ranges commonly between 0.3 mm and 0.8 in adults [40]. Hence, we set the thickness of the dura layer to 0.5 mm. The thicknesses of the skull and the width of the subarachnoid space (SAS) are filled with the cerebrospinal fluid (CSF) depend upon the individual and the location. Thus, we followed our previous approach [37], where we established averaged values for the thickness of the skull and CSF layers based on the dimensions measured from the cross section slices of the anatomical head model of an adult male provided by ANSYS. The simulation utilized frequency-dependent electrical properties of the head tissues. Table 1 summarizes the relative permittivity ($\varepsilon_r$) and conductivity ($\sigma$) of the head tissues using the four-term Cole-Cole relaxation model for capturing their frequency dependency and the thickness we applied in the model [41]. It is worth noting that different methodologies have been studied in the literature survey for designing and modeling the implantable antennas [1, 8, 15, 17, 42]. Among these, we have found the 7-layer human head model, which we have used in this work and our previous numerical studies [30–32], a computationally efficient model with sufficient prediction accuracy for the development of brain-implantable antennas.

Even though the 7-layer structure is easy to create in HFSS, it is very hard to implement a head phantom formed with the exact shape and thicknesses of tissue layers in practice. Achieving the desired dielectric properties with high accuracy is yet another challenge. Thus, for the better control of uncertainty, in the experiments, we used tissue-mimicking liquid. For this purpose, we filled a plastic truncated cone-shaped container (height = 13.5 cm, upper

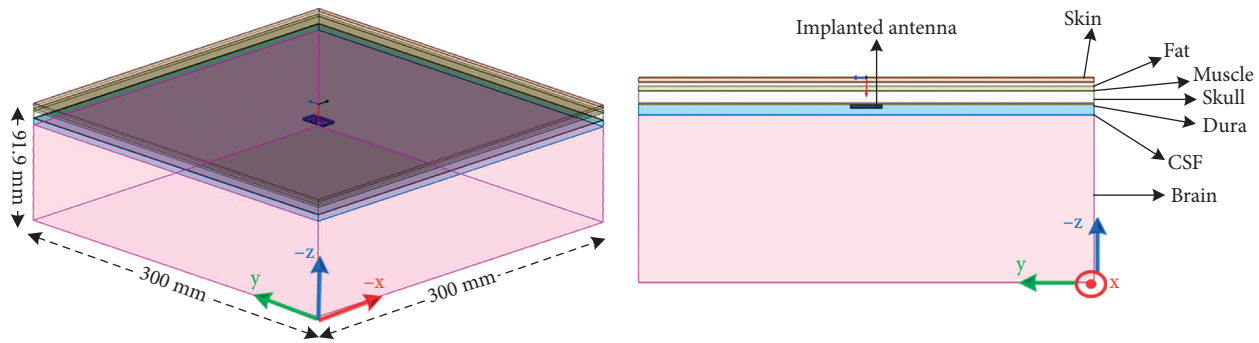


Figure 3: The 7-layer human head model used for the proposed implanted PIFA.

Table 1: Electrical properties of the 7-layer head model.

| Tissue | Thickness (mm) | 402 MHz | | 902 MHz | | 2400 MHz | |
|---|---|---|---|---|---|---|---|
| | | $\varepsilon_r$ | $\sigma$ (S/m) | $\varepsilon_r$ | $\sigma$ (S/m) | $\varepsilon_r$ | $\sigma$ (S/m) |
| Skin | 2 | 46.7 | 0.7 | 41.4 | 0.9 | 38.1 | 1.4 |
| Fat | 2 | 5.6 | 0.04 | 5.5 | 0.05 | 5.3 | 0.1 |
| Muscle | 2 | 57.1 | 0.8 | 55 | 0.9 | 52.8 | 1.78 |
| Skull | 5.5 | 20.3 | 0.2 | 19.6 | 0.3 | 18 | 0.8 |
| Dura | 0.5 | 46.6 | 0.8 | 44.4 | 0.96 | 42.1 | 1.68 |
| CSF | 4.9 | 71 | 2.3 | 68.6 | 2.4 | 66.3 | 3.48 |
| Brain (grey matter) | 75 | 57.4 | 0.7 | 52.7 | 0.9 | 49 | 1.8 |

radius = 8.5 cm, lower radius = 5.5 cm) with the commercial MVG's homogeneous liquid phantom for both MedRadio and ISM bands. The liquid phantom has the electrical properties of $\varepsilon_r = 43.56$, $\sigma = 0.91$ S/m at 402 MHz, $\varepsilon_r = 40.89$, and $\sigma = 0.98$ S/m at 902 MHz, and $\varepsilon_r = 38.59$ and $\sigma = 1.74$ S/m at 2400 MHz. To compare the measurement and simulation results, we replicated the liquid phantom in HFSS. For this purpose, we created the same shape of the employed plastic container in the HFSS, as demonstrated in Figure 4.

*2.3. Antenna Optimization.* To develop the initial antenna model located in the 7-layer head model and tune the desired operating frequencies, we assessed all critical design parameters, including the lengths of the meandered slots and shorting strip and the placement of the feeding pin. As observed from Figures 5(a)–5(c), truncating the length of the cutting slots ($l_1$, $l_3$, $l_5$) creates very high frequency bandwidth. In contrast, lengthening of the shorting strip ($l_6$) lowers the resonance frequencies at low- and midband frequency ranges specifically at 902 MHz, as shown in Figure 6(a). Simultaneously, by varying the distance between the shorting strip and feeding probe ($d$), we can control the magnitude of the reflection coefficient, as demonstrated in Figure 6(b). Following these principles, we set up parametric sweeps including these key design parameters in HFSS for further assessments. This way, we were eventually able to impedance-tune the antenna for the three frequencies by controlling only these geometrical parameters (($l_1$, $l_3$, $l_5$), $l_6$, and $d$) [32]. The antenna we selected for manufacturing and testing has the dimensions shown in Figure 2(b). In the simulation, it resonated at the frequencies of 390 MHz, 902 MHz, and 2430 MHz with the corresponding input reflection coefficient values of −8.1 dB, −9.2 dB, and −15.8 dB.

## 3. Measurement Setups, Results, and Discussion

*3.1. Prototype Fabrication.* Figure 7(a) displays the manufactured prototype layers on Rogers RO3210 substrate with 0.635 mm thickness. To assemble the antenna, first, we made a shorting strip by a high accuracy cutting of 1 mm width copper foil to connect the radiating patch to the ground plane. Then, we soldered the outer conductor of a 50-Ω RG178 RF coaxial cable to the ground layer and its inner conductor to the radiator for feeding. After that, as shown in Figure 7(b), we aligned the layers and glued them with a negligible layer thickness. In the end, we coated the prototype with biocompatible silicone. Thus, the total thickness of the structure after the coating approached 1.8 mm.

*3.2. Phantom Setup and Antenna Testing Procedure.* Figure 7(c) displays the phantom setup for testing the developed antenna. We attached a small plastic tube with a height of 13.25 mm in the center of a plastic truncated cone-shaped container to support the prototyped antenna within the liquid phantom. As shown in Figure 7(c), the RF coaxial cable connector was brought out through a small hole in the container's bottom and sealed with silicone. To test the fabricated antenna at both MedRadio and ISM bands, we filled the container every time with liquid for the desired frequency ranges. At first, as demonstrated in Figure 7(d), we measured the prototype antenna's input reflection

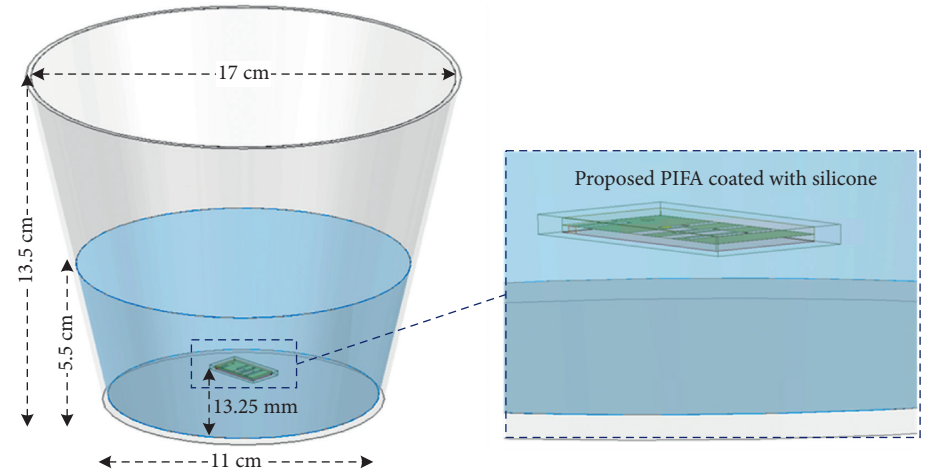


Figure 4: Simulation setup for placing the implanted PIFA in a plastic truncated cone-shaped container with the commercial MVG's homogeneous liquid phantom.

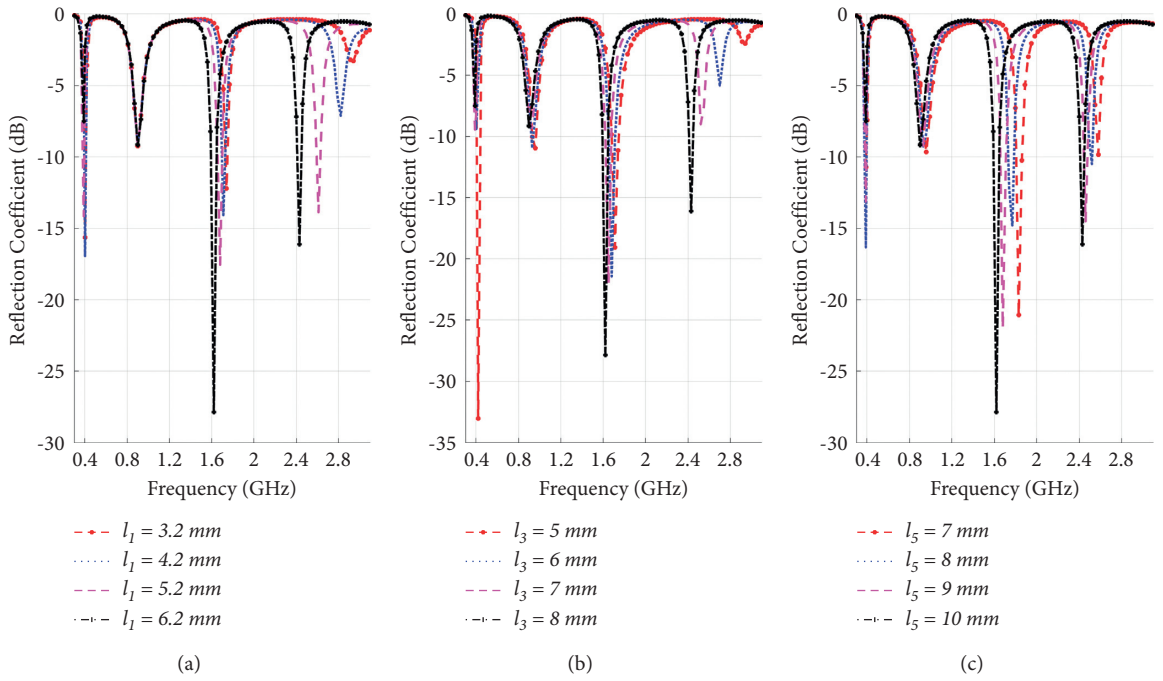


Figure 5: Effect of shortening the cutting slots of (a) $l_1$, (b) $l_3$, and (c) $l_5$.

coefficient using Vector Network Analyzer (VNA) to assess its impedance matching at the target frequencies of 402, 902, and 2400 MHz. Figure 8 compares the impedance matching of the triple-resonant antenna in simulation and measurement results. As is clear, the results agree well at the MedRadio band (402 MHz) and the lower resonant frequencies of the ISM band (902 MHz). In contrast, the higher operating frequencies of the ISM band (2400 MHz) shifted slightly to the upper resonances. Indeed, a slight difference in the permittivity and conductivity of liquid phantoms for different frequency bands leads to moving the measured impedance matching at the higher ISM band, as is evident in Figure 8, and influences the reflection coefficient magnitude. Moreover, the difficulty of controlling the silicone coating thickness in practice significantly impacts impedance matching at the highest resonance frequency.

In the next step, the radiation properties of the antenna were studied in the liquid phantom. For this purpose, we employed two different antenna measurement systems: an anechoic chamber with a standard far-field measurement system (ETS-Lindgren RF shielded enclosures) for MedRadio band and a near field measurement system (SATIMO Starlab anechoic chamber) for ISM bands. The anechoic chamber was used for the far-field measurements at a 3-meters testing distance for lower frequencies up to 550 MHz. Figure 9(a) demonstrates the measurement setup

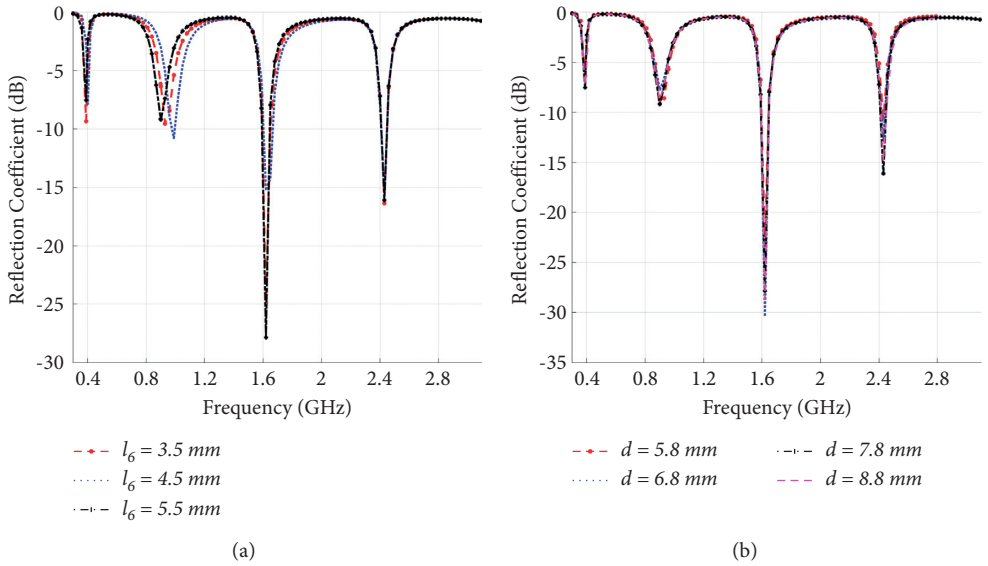


Figure 6: (a) Effect of increasing the length of $l_6$, (b) varying the distance between the shorting strip and feeding probe ($d$).

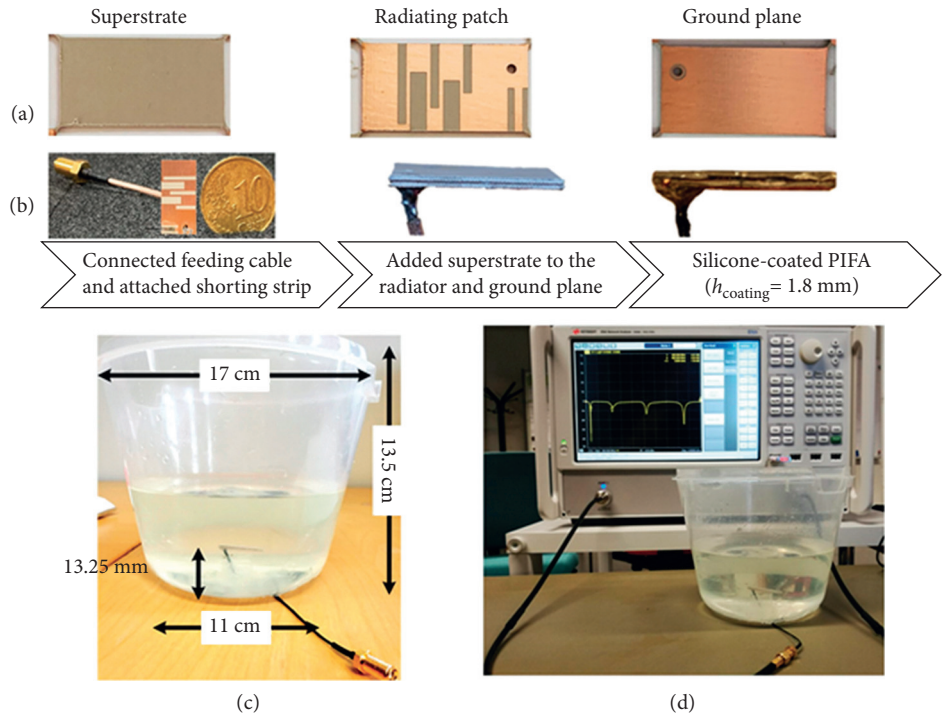


Figure 7: The prototyped PIFA. (a) Prototyped PIFA layers. (b) Assembled PIFA with feeding cable. (c) Phantom setup for testing of PIFA using a plastic truncated cone-shaped container. (d) Impedance matching measurement using VNA.

in an anechoic chamber for testing of PIFA at MedRadio band (402 MHz) located on a standing foam as high as the transmitting antenna (Yagi antenna). After that, the assembled antenna in head SAR liquid was tested in a SATIMO Starlab anechoic chamber for the ISM bands (902 and 2400 MHz). Figure 9(b) shows the measurement setup in the SATIMO Starlab chamber for the antenna placed in both liquid phantom of 900 and 2400 MHz at a depth of 13.25 mm. This measurement system utilizes several near-field probes to sample the antenna near field and then converts the near field data to the far-field antenna parameters. Figure 10 shows the 2D simulated (in the CSF region and the plastic container with liquid) and the measured antenna gain pattern at both XZ (phi = 0) and YZ (phi = 90) planes for the operating frequencies of 402, 902, and 2400 MHz. However, due to the measurement limitation at an anechoic chamber for MedRadio band, we were not able to present the measured gain pattern at the YZ plane for a resonant frequency of 402 MHz.

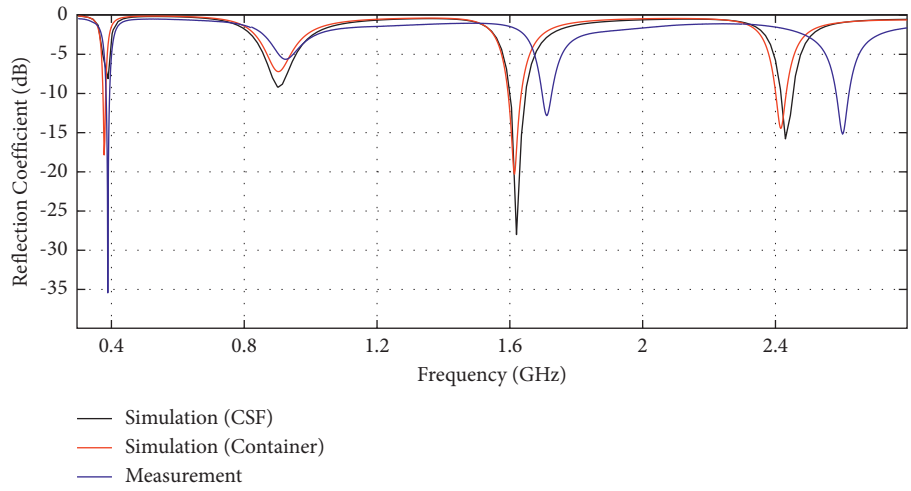


Figure 8: Comparison of the simulated and measured reflection coefficient ($S_{11}$).

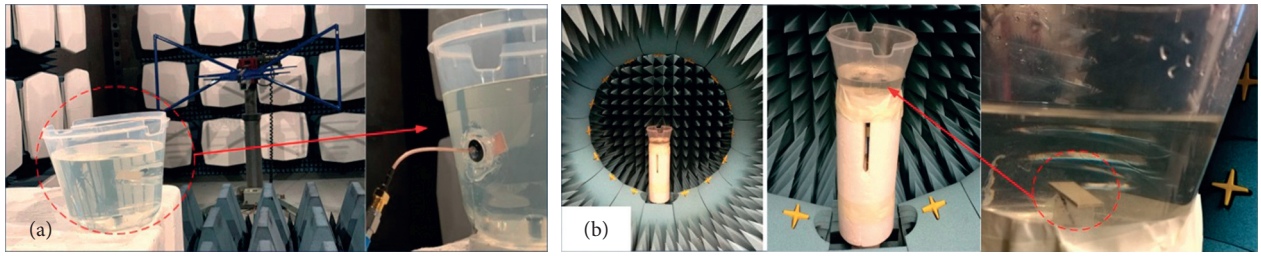


Figure 9: Measurement setup of implantable PIFA in liquid at the depth of 13.25 mm in (a) anechoic chamber and (b) SATIMO Starlab anechoic chamber.

To provide a proper visualization of the antenna radiation performance, Figures 11(a)–11(c) illustrate the 2D simulated co- and cross-polarization of the antenna gain pattern in the CSF layer and container at both XZ (phi = 0) and YZ planes (phi = 90) for resonant frequencies of 402, 902, and 2400 MHz. Moreover, Figures 12(a)–12(c) demonstrate the 3D simulated directivity in 7-layer head tissues. It is evident from the results that the proposed antenna attained good directivity in the direction outwards the human head tissues (along the −z-axis or at 180° in Figures 10–12). As shown in Figure 11, the simulated cross-polarization levels in the CSF layer at the antenna peak directivity (–z-axis (180°)) are 15.8, 31.8, and 28.4 dB less than the copolarization levels at resonant frequencies of 402, 902, and 2400 MHz, respectively, for both XZ and YZ planes. Similarly, the difference between simulated cross-polarization and copolarization levels in the container (in–z-axis direction) are 18.8, 17.9, and 8.1 dB at 402, 902, and 2400 MHz, respectively, for both XZ and YZ planes.

Subsequently, we studied the realized gain ($G_R$) of the antenna computed from the antenna gain ($G$) as $G_R = G(1-|S_{11}|^2)$. As shown in Figure 13, the measured and simulated realized gain of the antenna are in an appropriate agreement, especially near the targeted operation frequencies. Moreover, the realized gain exhibits local maxima near the targeted operation frequencies, verifying that the impedance matching has been achieved without compromising the antenna gain. At a frequency of 402 | 902 | 2400 MHz, the realized gain of the antenna is –45.6 | –27.6 | –25.4 dBi. Table 2 lists the corresponding antenna gain values ($G = G_R/(1-|S_{11}|^2)$), which exclude the impedance mismatch of the prototype antenna at these frequencies (see Figure 8) for a universal comparison and the percentage radiation efficiency.

The human tissue surrounding the implanted antenna absorbs part of the radiated electromagnetic energy. Therefore, for safety concerns, it is crucial to evaluate the specific absorption rate (SAR) for determining the maximum allowable net-input power to the antenna. To this end, SAR values must conform to IEEE C95.1–1999 (FCC) [43] and IEEE C95.1–2005 (ERC) [44] restricting the maximum average SAR over 1 g and 10 g of tissue mass to 1.6 W/kg and 2 W/kg, respectively. Additionally, according to FCC and ETSI standards and regulations, the emission limits of the effective isotropic radiated power (EIRP) are 25 $\mu$W (–16 dBm) for the frequency range of 402–405 MHz [45] and 6.3 mW (8 dBm) for the resonant band of 902–928 MHz and 100 mW (20 dBm) for 2400 MHz in wireless telemetry medical devices [46]. Given the gain values of our antenna presented in Table 2, it is clear that the maximum transmission power under the EIRP limits at 902 MHz and 2400 MHz will be very high for our application. At 402 MHz, the value is 173 mW for

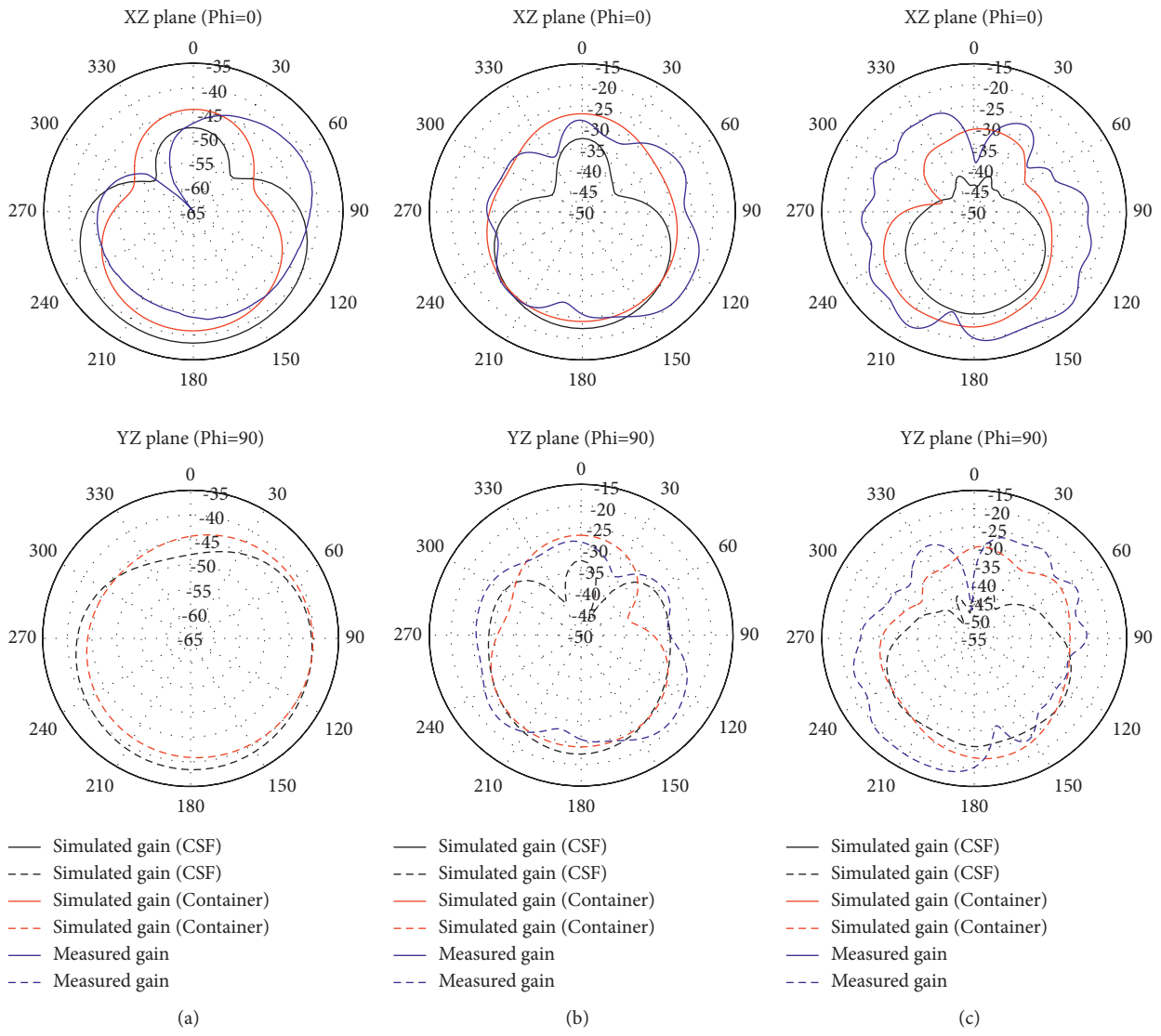


Figure 10: Simulated and measured antenna gain (dBi) pattern at the XZ plane and YZ plane for the frequency of (a) 402 MHz, (b) 902 MHz, and (c) 2400 MHz.

the simulated gain of −38.4 dBi. Next, we analyzed the average SAR numerically for the antenna implanted in the 7-layer head model by transmitting 1 W. Figure 14 visualizes the 1 g-averaged (1 g-avg) and 10 g-averaged (10 g-avg) SAR distribution within the simulation model at the operating frequencies of 402, 902, and 2400 MHz. Table 3 lists the simulated SAR values and the corresponding maximum transmission power levels. The data shows that the SAR regulations are more restrictive than the EIRP limits for the transmission power in all cases. Nonetheless, even the lowest transmission power of 5.9 mW can be considered high for the applications where the wireless implant communications is based on a low-power radio system.

Figure 15 compares the gain of various implantable antennas versus the electrical size ($ka$) at their lowest operating frequency. Generally, the antennas are categorized as electrically small when $ka \leq 0.5$, where $k = 2\pi/\lambda$ is the free space wavenumber and $a$ is the radius of the smallest sphere enclosing the antenna [33]. As illustrated in Figure 15, among green markers for 9 mm < implant depth ≤15 mm, the proposed antenna is the only triple-band antenna. Additionally, multiband antennas with lower $ka$ are at the maximum depth of 5 mm compared to our antenna placed at the depth of 13.25 mm. Furthermore, the reported multiband antenna in [18] with higher gain features has higher $ka$ compared to our antenna. Table 4 compares our antenna with other similar works in terms of the antenna gain. From the comparison, we conclude that our antenna achieves and partly exceeds the state-of-the-art radiation performance, while the implant location we have considered is deeper than in the compared works, excluding [38] where a single-band implant antenna was studied at the depth of 16 mm. In addition, all other triple-band antennas have been studied in skin which is far less lossy environment than CSF (see Table 1).

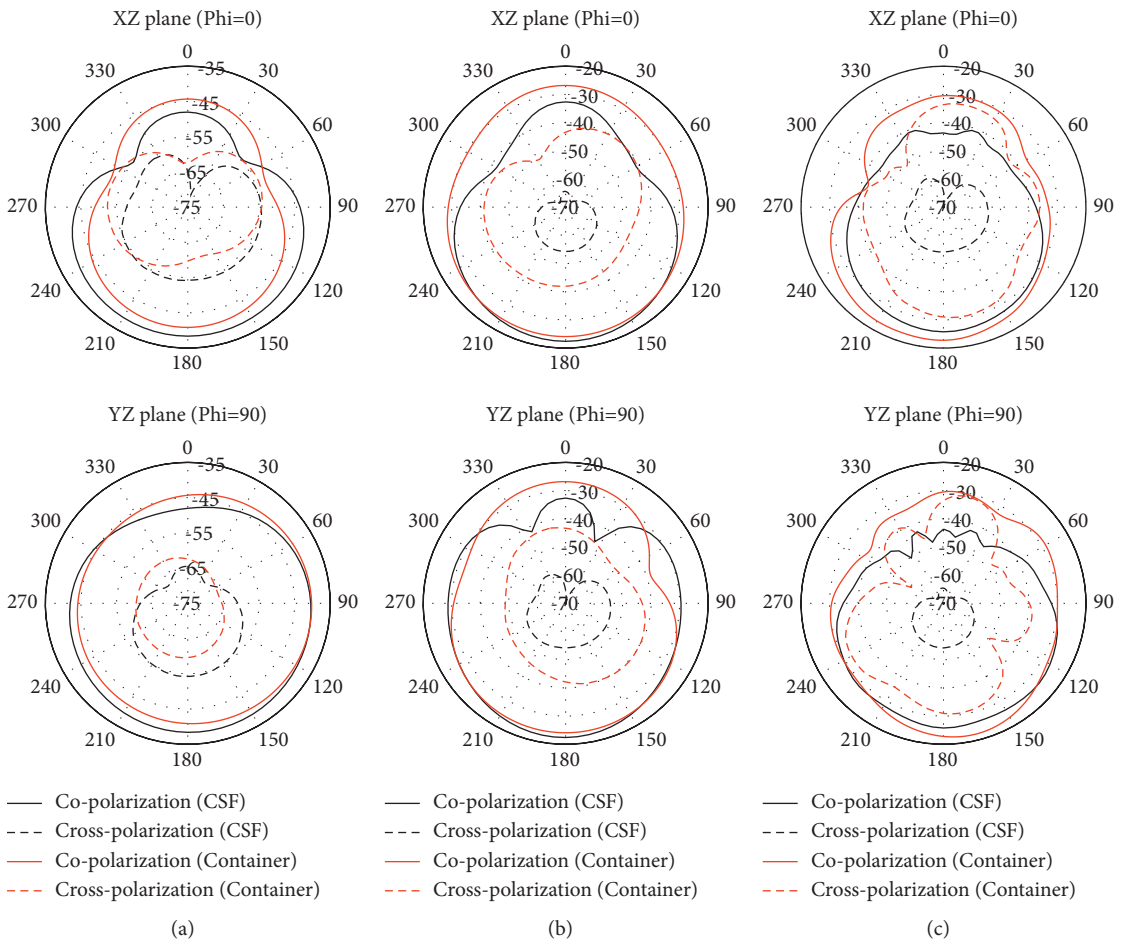


Figure 11: 2D simulated co- and cross-polarization of the antenna gain pattern (dBi) in 7-layer head model and container at the XZ plane and YZ plane. (a) 402 MHz, (b) 902 MHz, and (c) 2400 MHz.

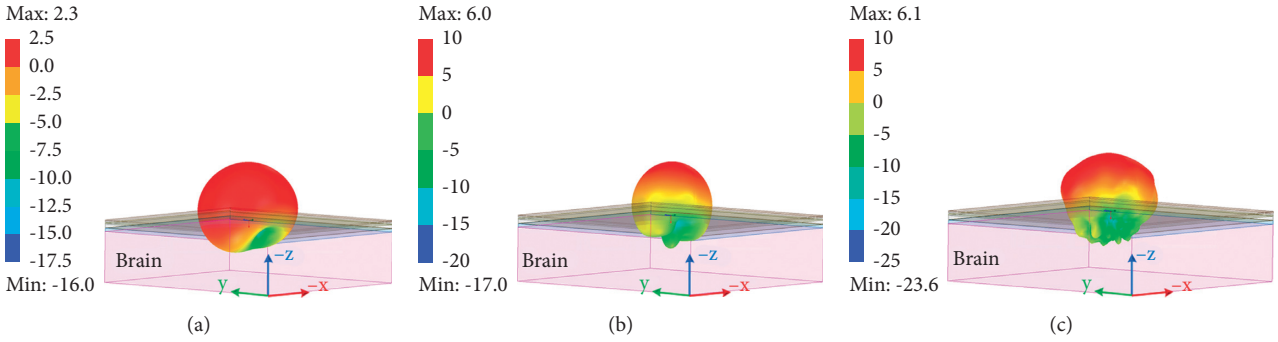


Figure 12: 3D simulated antenna directivity: (a) 402 MHz, (b) 902 MHz, and (c) 2400 MHz.

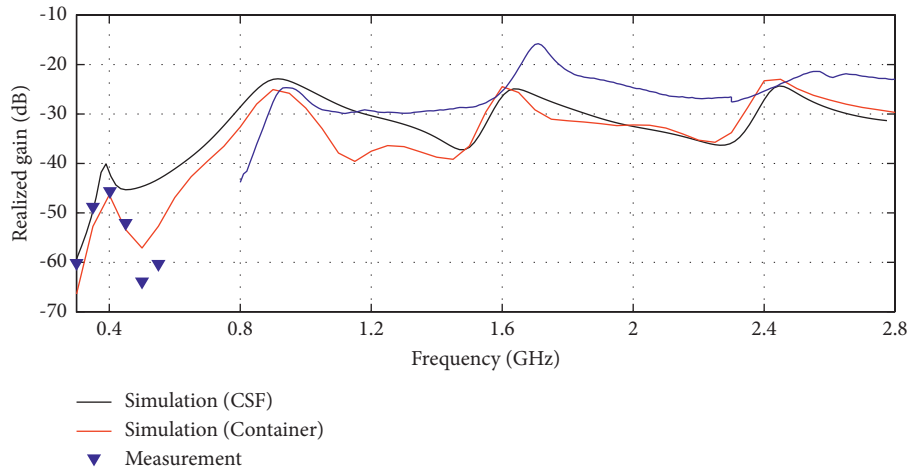


Figure 13: Simulated and measured realized gain of the implantable PIFA.

Table 2: Antenna gain (dBi) and radiation efficiency (%).

| | 402 MHz<br>Gain \| RE | 902 MHz<br>Gain \| RE | 2.4 GHz<br>Gain \| RE |
|---|---|---|---|
| Sim/CSF | −38.4 \| 0.01 | −22.4 \| 0.10 | −25.8 \| 0.10 |
| Sim/container | −40.9 \| 0.01 | −24.1 \| 0.20 | −22.8 \| 0.10 |
| Measured | −43.6 \| N/A | −25.8 \| 0.40 | −20.1 \| 1.30 |

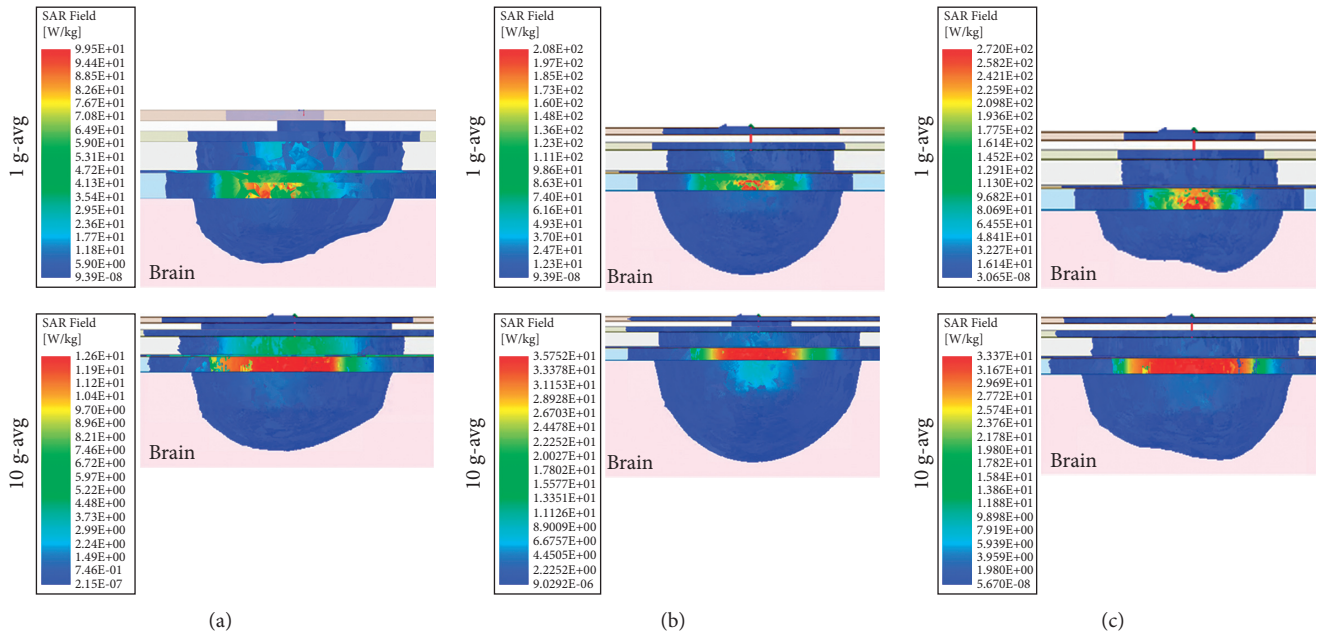


Figure 14: Simulated distribution of 1 g-avg and 10 g-avg SAR for the 7-layer human head model. (a) 402 MHz, (b) 902 MHz, and (c) 2400 MHz.

Table 3: Simulated maximum average SAR values for 1 W input power and maximum allowable input power.

| Frequency (MHz) | Maximum SAR (W/kg) | | Maximum allowable input power (mW) | |
|---|---|---|---|---|
| | 1 g-avg | 10 g-avg | C95.1–1999 (SAR <1.6 W/kg) | C95.1–2005 (SAR <2 W/kg) |
| 402 | 99.5 | 12.6 | 16.1 | 159 |
| 902 | 207.8 | 35.8 | 7.7 | 56 |
| 2400 | 272 | 33.4 | 5.9 | 60 |

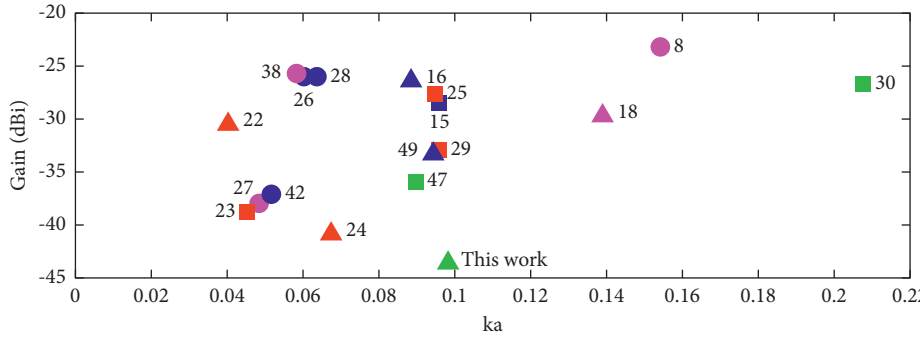


Figure 15: Comparison of implantable antennas' gain versus electrical size ($ka$). The red, blue, green, and purple markers, respectively, are used for the implant depth <3 mm, 3 mm < implant depth ≤9 mm, 9 mm < implant depth ≤15 mm, and implant depth >15 mm. Circle, square, and triangle markers indicate single-, dual-, and multiband implantable antennas, respectively. The numbers in the figure refer to the list of references.

Table 4: Comparison of implantable antennas.

| Ref. | Type | Frequency (MHz) | Volume ($mm^3$) | Implant depth | Gain (dBi) | Short pin | SAR (W/kg) | |
|---|---|---|---|---|---|---|---|---|
| | | | | | | | 1 g | 10 g |
| [16] | PIFA | 915 | $7 \times 6 \times 0.5$ | 4.5 mm in skin | −26.4 | Yes | 380 | 40.4 |
| | | 1900 | | | −23 | | 358 | 38.2 |
| | | 2450 | | | −20.47 | | 363 | 40.3 |
| [22] | Patch | 402 | $7 \times 6.5 \times 0.377$ | 3 mm in scalp | −30.5 | No | 588 | 92.7 |
| | | 1600 | | | −22.5 | | 441 | 85.3 |
| | | 2450 | | | −18.2 | | 305 | 81.7 |
| [23] | PIFA | 402 | $9 \times 11 \times 0.5$ | 3 mm in skin | −38.8 | Yes | 719 | –– |
| | | 2450 | | | −18.6 | | 746 | –– |
| [24] | PIFA | 405 | $14 \times 7.5 \times 0.5$ | 3 mm in scalp | −40.85 | Yes | 665.35 | 93.24 |
| | | 915 | | | −32.98 | | 837.69 | 93.97 |
| | | 2450 | | | −22.37 | | 759.72 | 87.24 |
| [38] | Split ring | 915 | $\pi \times (3 \times 1.5) \times 1$ | 16 mm in CSF | −25.7 | No | –– | –– |
| [47] | PIFA | 402 | $16 \times 14 \times 1.27$ | 10 mm in muscle | −35.9 | Yes | –– | –– |
| | | 915 | | | −24.3 | | –– | –– |
| [48] | Patch | 2450 | $10 \times 10 \times 0.5$ | 12 mm in CSF | −25 | No | –– | –– |
| | | | | | | | –– | –– |
| [49] | PIFA | 402 | $\pi \times (11.2)^2 \times 0.5$ | 4 mm in head | −33.3 | Yes | 241 | –– |
| | | 1430 | | | −21.9 | | 269 | –– |
| | | 2450 | | | −19.6 | | 290 | –– |
| This work | PIFA | 402 | $11 \times 20.5 \times 1.8$ | 13.25 mm in CSF | −43.6 | Yes | 99.5 | 12.6 |
| | | 902 | | | −25.8 | | 207.8 | 35.8 |
| | | 2400 | | | −20.1 | | 272 | 33.4 |

## 4. Conclusions

Wireless brain care that is based on medical implants is a novel approach in the biomedical field. It is enabled by small antennas. In this paper, we presented an implantable PIFA that is targeted for the MedRadio (402 MHz) and ISM (902 and 2400 MHz) bands. It is self-matched to the impedance of 50 Ω. By patterning meandered slots in the radiator and shorting it to the ground, we downsized the antenna to the volume of $11 \times 20.5 \times 1.8\ mm^3$. We optimized its electromagnetic performance through the full-wave EM simulations in a 7-layer head model and tested it in a tissue-mimicking liquid. The implant depth we have considered is beyond most prior works, whereas the gain of our design reached the state-of-the-art. In the future, we will study the impact of the changing operating environment on the antenna's performance and explore how to control its fourth resonance frequency.

## Data Availability

The presented data and results in this study are available from the corresponding author upon request.

## Conflicts of Interest

The authors declare that there are no conflicts of interest regarding the publication of this paper.

## Acknowledgments

This research was funded by the Doctoral Programme in Biomedical Sciences and Engineering under the Faculty of Medicine and Health Technology of Tampere University, Academy of Finland under funding decision 294616, and supported by the Finnish Foundation for Technology Promotion (TES) and Nokia Foundation.

## References

[1] Y. Rahmat-Samii and E. Topsakal, *Antenna and Sensor Technologies in Modern Medical Applications*, Wiley, Hoboken, NJ, USA, 2021.

[2] Y. Rahmat-Samii and J. Kim, "Implanted antennas in medical wireless communications," *Synthesis Lectures on Antennas*, vol. 1, no. 1, pp. 1–82, 2006.

[3] C. Liu, Y. Guo, and S. Xio, "A review of implantable antennas for wireless biomedical devices," *Forum for Electromagnetic Research Methods and Application Technologies (FERMAT)*, vol. 14, no. 3, pp. 1–11, 2016.

[4] M. Chen, S. Gonzales, A. Vasilakos, H. Cao, and V. C. M. Leung, "Body-area networks: a survey," *Mobile Networks and Applications*, vol. 16, no. 2, 2011.

[5] Y.-L. Zheng, X.-R. Ding, C. C. Y. Lo et al., "Unobtrusive sensing and wearable devices for health informatics," *IEEE Transactions on Biomedical Engineering*, vol. 61, no. 5, pp. 1538–1554, 2014.

[6] J. Andreu-Perez, D. R. Leff, H. M. D. Ip, and G. Yang, "From wearable sensors to smart implants–toward pervasive and personalized healthcare," *IEEE Transactions on Biomedical Engineering*, vol. 62, no. 12, 2015.

[7] M. R. Jan, "Towards TRUE human-centric computation," *Computer and Communications*, vol. 131, pp. 73–76, 2018.

[8] H. Li, B. Wang, L. Guo, and J. Xiong, "Efficient and wideband implantable antenna based on magnetic structures," *IEEE Transactions on Antennas and Propagation*, vol. 67, no. 12, pp. 7242–7251, 2019.

[9] D. Nikolayev, M. Zhadobov, P. Karban, and R. Sauleau, "Electromagnetic radiation efficiency of body-implanted devices," *Physical Review Applied*, vol. 9, no. 2, p. 12, 2018.

[10] A. K. Skrivervik, M. Bosiljevac, and Z. Sipus, "Fundamental limits for implanted antennas: maximum power density reaching free space," *IEEE Transactions on Antennas and Propagation*, vol. 67, no. 8, pp. 4978–4988, 2019.

[11] M. Zaiembashi, H. Lin, C. Dong et al., "NanoNeuroRFID: A wireless implantable device based on magnetoelectric antennas," *IEEE Journal of Electromagnetics, RF and Microwaves in Medicine and Biology*, vol. 3, no. 3, pp. 206–215, 2019.

[12] Y. El-Saboni, D. E. Zelenchuk, G. A. Conway, and W. G. Scanlon, "Assessing the intrinsic radiation efficiency of tissue-implanted UHF antennas," *IEEE Transactions on Antennas and Propagation*, vol. 68, no. 1, pp. 491–499, 2020.

[13] Z. Sipus, A. Susnjara, A. K. Skrivervik, D. Poljak, and M. Bosiljevac, "Influence of uncertainty of body permittivity on achievable radiation efficiency of implantable Antennas–stochastic analysis," *IEEE Transactions on Antennas and Propagation*12 pages. In press, 2021.

[14] S. Bakogianni and S. Koulouridis, "On the design of miniature MedRadio implantable antennas," *IEEE Transactions on Antennas and Propagation*, vol. 65, no. 7, pp. 3447–3455, 2017.

[15] S. A. A. Shah and H. Yoo, "Scalp-implantable antenna systems for intracranial pressure monitoring," *IEEE Transactions on Antennas and Propagation*, vol. 66, no. 4, pp. 2170–2173, 2018.

[16] M. Zada and H. Yoo, "A miniaturized triple-band implantable antenna system for bio-telemetry applications," *IEEE Transactions on Antennas and Propagation*, vol. 66, no. 12, pp. 7378–7382, 2018.

[17] G. Samanta and D. Mitra, "Dual-band circular polarized flexible implantable antenna using reactive impedance substrate," *IEEE Transactions on Antennas and Propagation*, vol. 67, no. 6, pp. 4218–4223, 2019.

[18] Z. Bao, Y.-X. Guo, and R. Mittra, "Single-layer dual-/tri-band inverted-F antennas for conformal capsule type of applications," *IEEE Transactions on Antennas and Propagation*, vol. 65, no. 12, pp. 7257–7265, 2017.

[19] Y. Fan, X. Liu, J. Li, and T. Chang, "A miniaturized circularly-polarized antenna for in-body wireless communications," *Micromachines*, vol. 10, 2019.

[20] Y. Zhang, C. Liu, X. Liu, K. Zhang, and X. Yang, "A wideband circularly polarized implantable antenna for 915 MHz ISM-band biotelemetry devices," *IEEE Antennas and Wireless Propagation Letters*, vol. 17, no. 8, pp. 1473–1477, 2018.

[21] G. Samanta and D. Mitra, "Miniaturised and radiation efficient implantable antenna using reactive impedance surface for biotelemetry," *IET Microwaves, Antennas & Propagation*, vol. 14, no. 2, pp. 177–184, 2020.

[22] I. A. Shah, M. Zada, and H. Yoo, "Design and analysis of a compact-sized multiband spiral-shaped implantable antenna for scalp implantable and leadless pacemaker systems," *IEEE Transactions on Antennas and Propagation*, vol. 67, no. 6, pp. 4230–4234, 2019.

[23] J. Shang, Y. Yu, and L. J. Xu, "Compact dual-band implantable planar inverted-F antenna with bandwidth enhancement," *Microwave and Optical Technology Letters*, vol. 62, no. 1, pp. 322–328, 2020.

[24] I. Gani and H. Yoo, "Multi-band antenna system for skin implant," *IEEE Microwave and Wireless Components Letters*, vol. 26, no. 4, pp. 294–296, 2016.

[25] F. Faisal, M. Zada, A. Ejaz, Y. Amin, S. Ullah, and H. Yoo, "A miniaturized dual-band implantable antenna system for medical applications," *IEEE Transactions on Antennas and Propagation*, vol. 68, no. 2, pp. 1161–1165, 2020.

[26] W. C. Liu, F. M. Yeh, and M. Ghavami, "Miniaturized implantable broadband antenna for biotelemetry communication," *Microwave and Optical Technology Letters*, vol. 50, no. 9, pp. 2407–2409, 2008.

[27] W.-C. Liu, S.-H. Chen, and C.-M. Wu, "Bandwidth enhancement and size reduction of an implantable PIFA antenna for biotelemetry devices," *Microwave and Optical Technology Letters*, vol. 51, no. 3, pp. 755–757, 2009.

[28] C.-M. Lee, T.-C. Yo, C.-H. Luo, C.-H. Tu, and Y.-Z. Juang, "Compact broadband stacked implantable antenna for biotelemetry with medical devices," *Electronics Letters*, vol. 43, no. 12, pp. 660–662, 2007.

[29] D. Alptekin, L. Alatan, and N. G. Gençer, "Dual band PIFA design for biomedical applications," in *Proceedings of the Dual Band PIFA Design for Biomedical Applications (EuCAP)*, pp. 1–4, Davos, Switzerland, June 2016.

[30] N. Pournoori, S. Ma, and L. Sydänheimo, "Compact dual-band PIFA based on a slotted radiator for wireless biomedical implants," in *Proceedings of the 2019 IEEE International Symposium on Antennas and Propagation and USNC-URSI Radio Science Meeting*, pp. 13-14, Atlanta, GA, USA, April 2019.

[31] N. Pournoori, S. Ma, and L. Sydänheimo, "Small multi-resonant meandered PIFA for brain implant communications," in *Proceedings of the 2019 8th Asia-Pacific Conference on*

*Antennas and Propagation (APCAP)*, p. 3, Incheon, Korea (South), August 2019.

[32] N. Pournoori, S. Ma, L. Sydänheimo, Y. Rahmat-Samii, L. Ukkonen, and T. Björninen, "Compact multi-band PIFA with meandered radiator for wireless brain implant communication," in *Proceedings of the XXXV Finnish URSI Convention on Radio Science*, URSI, Tampere, Finland, October 2019.

[33] C. A. Balanis, *Antenna Theory: Analysis and Design*, Wiley, Hoboken, NJ, USA, 2005.

[34] Z. D. Zi Dong Liu, P. S. Hall, and D. Wake, "Dual-frequency planar inverted-F antenna," *IEEE Transactions on Antennas and Propagation*, vol. 45, no. 10, pp. 1451–1458, 1997.

[35] H. T. Chattha, M. K. Ishfaq, Y. Huang, and S. J. Boyes, "Band-notched ultrawide band planar inverted-F antenna," *International Journal of Antennas and Propagation*, vol. 2012, no. 1, 6 pages, Article ID 513829, 2012.

[36] A. Elouadih, A. Oulad-Said, and M. Hassani, "Design and parametric simulation of a miniaturized PIFA antenna for the PCS band," *Wireless Engineering and Technology*, vol. 4, no. 2, pp. 105–111, 2013.

[37] S. Ma, L. Sydanheimo, L. Ukkonen, and T. Bjorninen, "Split-ring resonator antenna system with cortical implant and head-worn parts for effective far-field implant communications," *IEEE Antennas and Wireless Propagation Letters*, vol. 17, no. 4, pp. 710–713, 2018.

[38] S. Ma, T. Bjorninen, L. Sydanheimo, M. H. Voutilainen, and L. Ukkonen, "Double split rings as extremely small and tuneable antennas for brain implantable wireless medical microsystems," *IEEE Transactions on Antennas and Propagation*, vol. 69, no. 2, pp. 760–768, 2021.

[39] A. Drossos, V. Santomaa, and N. Kuster, "The dependence of electromagnetic energy absorption upon human head tissue composition in the frequency range of 300-3000 MHz," *IEEE Transactions on Microwave Theory and Techniques*, vol. 48, no. 11, pp. 1988–1995, 2000.

[40] A. N. Bashkatov, E. A. Genina, Y. P. Sinichkin, V. I. Kochubey, N. A. Lakodina, and V. V. Tuchin, "Glucose and mannitol diffusion in human dura mater," *Biophysical Journal*, vol. 85, no. 5, pp. 3310–3318, 2003.

[41] S. Gabriel, R. W. Lau, and C. Gabriel, "The dielectric properties of biological tissues: III. Parametric models for the dielectric spectrum of tissues," *Physics in Medicine and Biology*, vol. 41, no. 11, pp. 2271–2293, 1996.

[42] A. Kiourti and K. S. Nikita, "Implantable antennas: a tutorial on design, fabrication, and in vitro in vivo testing," *IEEE Microwave Magazine*, vol. 15, no. 4, pp. 77–91, 2014.

[43] IEEE, *IEEE Standard C95.1-1999, IEEE Standard for Safety Levels with Respect to Human Exposure to Radio Frequency Electromagnetic Fields, 3 kHz to 300 GHz*, IEEE, Piscataway, NJ, USA, 1999.

[44] IEEE, *Standard for safety levels with respect to human exposure to radio frequency electromagnetic fields, 3 kHz to 300 GHz, IEEE Standard C95.1-2005*, IEEE, Piscataway, NJ, USA, 2005.

[45] *F.C.C. Rules: CFR-47, Part-95*, MICS, Federal Communications Commission, Wireless Communications Office, Washington, DC, USA, 2006, http://wireless.fcc.gov/services/index.htm?job=service_home&id=medical_implant.

[46] *F.C.C.Rules: CFR Title-47, Part 18, ISM Equipment*, Federal Communications Commission, Wireless Communications Office, Washington, DC, USA, 2006, http://wireless.fcc.gov/cgibin/wtbbye.pl?http://www.access.gpo.gov/nara/cfr/waisidx_06/47cfr18_06.html.

[47] S. Bakogianni and S. Koulouridis, "A dual-band implantable rectenna for wireless data and power support at sub-GHz region," *IEEE Transactions on Antennas and Propagation*, vol. 67, no. 11, pp. 6800–6810, 2019.

[48] B. Rana, J.-Y. Shim, and J.-Y. Chung, "An implantable Antenna with broadside radiation for a brain-machine interface," *IEEE Sensors Journal*, vol. 19, no. 20, pp. 9200–9205, 2019.

[49] T.-A. Le Trong, S. I. H. Shah, G. Shin, S. M. Radha, and I.-J. Yoon, "A compact triple-band antenna with a broadside radiation characteristic for head-implantable wireless communications," *IEEE Antennas and Wireless Propagation Letters*5 pages. In press, 2021.